MCD of Non-aromatic Cyclic π-Electron Systems. Part 6: Pentalenes and Heptalenes

JÖRG FLEISCHHAUER,[1] GERHARD RAABE,[1] KENNETH A. KLINGENSMITH,[2] UDO HÖWELER,[2] PRABIR K. CHATTERJEE,[2] KLAUS HAFNER,[3] EMANUEL VOGEL,[4] JOSEF MICHL[2]

[1]*Institut für Organische Chemie, RWTH Aachen, Aachen, Germany*

[2]*Department of Chemistry and Biochemistry, University of Colorado, Boulder, Colorado 80309-0215, USA*

[3]*Technical University Darmstadt, Darmstadt, Germany*

[4]*University of Cologne, Cologne, Germany*

ABSTRACT: The magnetic circular dichroism (MCD) spectra of several stable derivatives of pentalene (**1**) and heptalene (**2**) have been recorded. The lowest energy transition (from the ground to the S state in perimeter model nomenclature) is extremely weak in MCD and in absorption. The sign patterns of the B terms for the first three strong transitions—N_1, N_2, P_1—in the order of increasing energy, are $--+$ for **1** and $++-$ for **2**. These findings are in perfect agreement with numerical results obtained at the SACCI level and with expectations based on the perimeter model of Parts 1–4 of this series, both of which lead to the conclusion that the magnetic mixing of the S excited state with the ground state is dominant. This is an extremely rare situation for an organic molecule, in which B term signs are normally determined by the mutual magnetic mixing of excited states. It can be expected to occur in other conjugated systems derived from $4N$-electron perimeters that have a low-energy first excitation, which is of intrashell nature in the perimeter model and therefore is magnetic-dipole allowed. In contrast, all low-energy transitions in the much more common systems derived from $(4N + 2)$-electron perimeters are of intershell nature and are magnetic-dipole forbidden. © 2005 Wiley Periodicals, Inc. Int J Quantum Chem 102: 925–939, 2005

Key words: magnetic circular dichroism; pentalene; heptalene; perimeter model

In Part 5 of this series [1], we examined the magnetic circular dichroism (MDC) of biphenylene and its heterocyclic analogs. The non-alternant pentalene (**1**) and heptalene (**2**) are additional prototype hydrocarbons of the "unaromatic" [2] kind, derived from antiaromatic 4N-electron perimeters by a cross-linking perturbation that significantly splits the nonbonding orbital pair. Over the years, their excited electronic states have been the subject of many calculations [3], including some recent ones [4–6]. However, primarily due to their very low stability, **1, 2,** and their derivatives have received little attention from spectroscopists. The ordinary absorption spectra of **2** [7] and of alkyl and aryl derivatives of **1** [8, 9] have been recorded, as has the UV absorption spectrum of **1** in matrix isolation [5]. The results are in qualitative agreement with expectations based on the simple 4N-electron perimeter model, introduced in Parts 1–4 of this series [2, 10–12] whose hallmarks are a low-energy region with an electric-dipole–forbidden but magnetic-dipole–allowed state (S) followed by a high-energy region containing two weakly (N_1, N_2) and two strongly (P_1, P_2) electric-dipole–allowed states and an entirely forbidden doubly excited state (D).

We are not aware of any prior measurements of MCD spectra of **1** and **2,** which would permit a more complete characterization of the electronic transitions. We now report the MCD of several stable derivatives of **1** and **2** and interpret them in terms of the perimeter model and of numerical calculations by CIS, TD-DFT, and SACCI methods. To our knowledge, **1** and **2** represent the first known organic molecules in which the usually negligible effects of the magnetic mixing of the ground and excited states actually determine the signs of low-energy B terms.
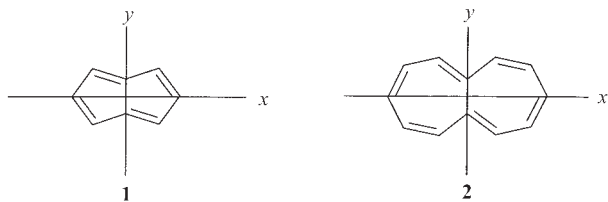
Experimental Part and Computations

The synthesis and purification of samples have been described elsewhere for dimethyl 1,3-di-t-butylpentalene-4,5-dicarboxylate [13], 3,8-dibromo-heptalene [14], dimethyl heptalene-3,8-dicarboxylate [15], dimethyl heptalene-1,2-dicarboxylate [16] and 1,2,5,6,8,10-hexamethylheptalene [17]. A slightly oxidized sample of 1,3,5-tri-t-butylpentalene [9] was also examined.

Cyclohexane (Aldrich Spectrograde) was passed over an Al_2O_3–$AgNO_3$ column prior to use. Absorption spectra were measured using a Varian Model 2300 Spectrophotometer. The MCD was measured using a JASCO J-600 Spectropolarimeter equipped with a 1.4 Tesla electromagnet and calibrated [18] against the CD of d-camphorsulfonic acid and the MCD of naphthalene. The MCD B terms were evaluated from the formula $B = -33.53^{-1} \int d\tilde{\nu}[\theta]_M/\tilde{\nu}$.

Calculations were performed at C_{2h} and D_{2h} constrained optimized (MP2/6-31+G*, Gaussian 03 [19]) geometries, using the CIS/TZVP [20] method (Gaussian 03 [19]), the TD-DFT method with the BP86 functional [21] and the TZVP basis set [20] (Turbomole [22]), and the SACCI [23] method with the DZP [24] basis set and an active space containing 20 occupied and 50 virtual orbitals; the sum in the computation of B terms was truncated to the first 32 excited states [25].

Results

SPECTRA

The absorption and MCD spectra of dimethyl 1,3-di-t-butylpentalene-4,5-dicarboxylate (**1A**), 3,8-dibromoheptalene (**2A**), dimethyl heptalene-3,8-dicarboxylate (**2B**), dimethyl heptalene-1,2-dicarboxylate (**2C**), and 1,2,5,6,8,10-hexamethylheptalene (**2D**) are summarized in Table I and shown in Figures 1 through 5. The spectrum of **1A** resembles that of the matrix-isolated parent **1,** except that it clearly shows a very weak band in the visible spectrum, which was not observed in the dilute matrix isolate sample, despite the authors' best efforts [5].

The spectra of all these pentalene and heptalene derivatives clearly have much in common. The most obvious feature they share is the presence of two fairly intense broad bands located approximately at 25,000–35,000 and 35,000–40,000 cm^{-1}. The higher-energy band is several times more intense; the difference is particularly pronounced in the undoubtedly strongly nonplanar hexamethyl derivative **2D,** in which most transitions are shifted to noticeably higher energies. The MCD signs of the two bands are opposite. The signal of the lower-energy band is positive (negative B term) in the

TABLE I _____

Electronic transitions in derivatives of 1 and 2.

Transition\Compound		1A	2A	2B	2C	2D
S	E^a	7–20	15–23	18–23	17–26	23–30
	int., B^b	vw, +0.03	vw, +vw	vw, +vw	vw, +vw	vw, +vw
N_1	E^a	~27	~28	~25	~29	~32
	int., B^b	m, $(-0.2)^c$	m, $(+2.2)^c$	m, $(+1.6)^c$	m, $(+3.4)^c$	m, $(+0.5)^c$
N_2	E^a	~32	~34	~30	~34	~35
	int., B^b	w, $(-0.2)^c$	m, $(+2.2)^c$	w, $(+1.6)^c$	w, $(+3.4)^c$	m, $(+0.5)^c$
P_1	E^a	~38	~36	~38	~37	~37
	int., B^b	s, +0.2	s, −1.1	s, −1.3	s, −2.6	s, −0.5
5	E^a	~41	~40			
	int., B^b	w, −0.03	w			
6	E^a	~46	~46	~47	~48	~47
	int., B^b	s, +0.8	s, +1.4	s, +2.3	s, +3.8	s, +2.2

[a] Units: 10^3 cm^{-1}.
[b] Units: 10^{-3} Debye^2 β_e/cm^{-1} (values are approximate).
[c] The sum of B terms of transitions N_1 and N_2.

pentalene derivative **1A** and negative (positive B term) in the heptalene derivatives **2A–2D.** The shape of the MCD spectrum in the region of the first
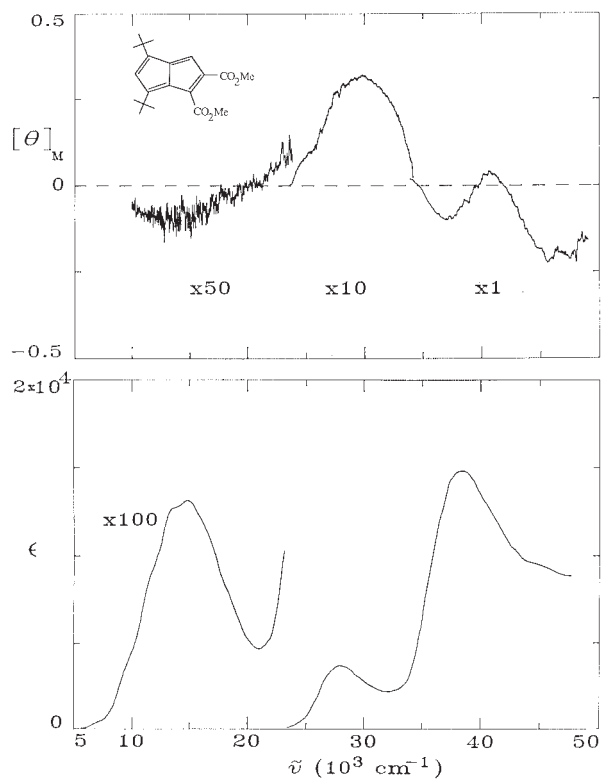

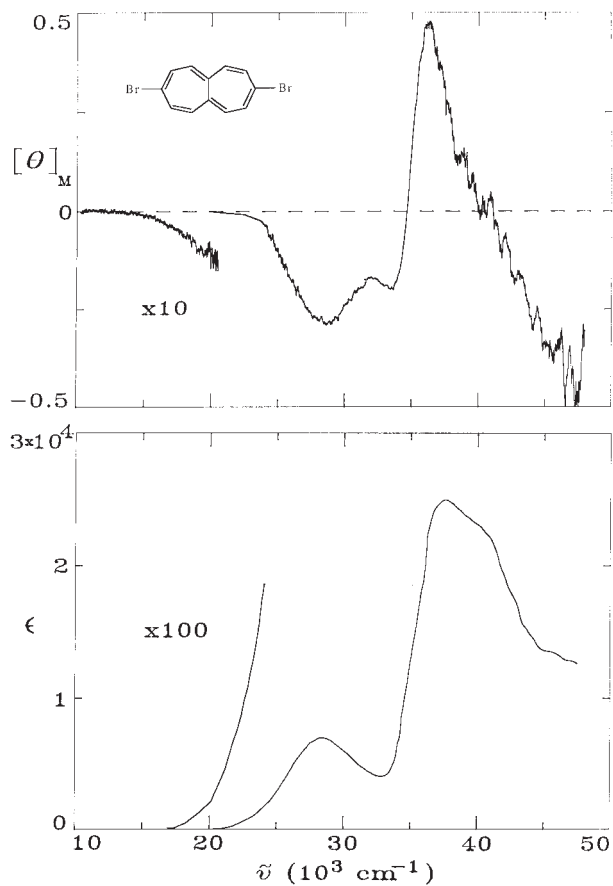**FIGURE 1.** Absorption (bottom) and MCD (top) of **1A** in cyclohexane.

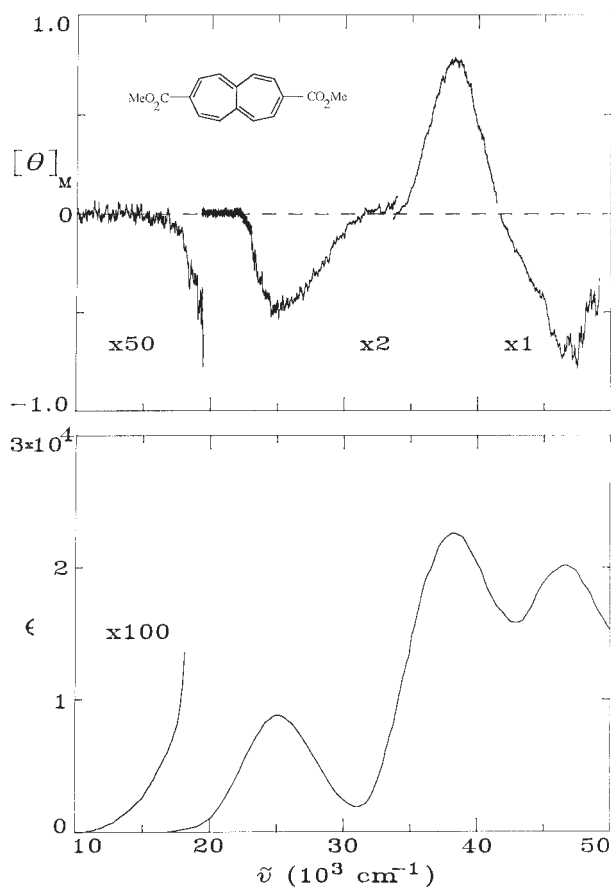**FIGURE 2.** Absorption (bottom) and MCD (top) of **2A** in cyclohexane.

FIGURE 3. Absorption (bottom) and MCD (top) of **2B** in cyclohexane.

strong broad band differs considerably from that of the absorption spectrum. This is most readily accounted for by accepting the literature assignment [5] of two transitions under the broad-band envelope. Their MCD signs are the same, but the B/D ratios differ (D is the transition dipole strength). The presence of two distinct transitions in the region of the first broad band is most clearly apparent in the MCD spectrum of **2A.** We conclude that the MCD signs of the three intense transitions are $--+$ for **1** and $++-$ for **2** in order of increasing energy.

The second common feature is the presence of a very weak absorption band at energies well below those of the lower of the above two bands. In most cases, it does not have a clear onset, and its presence is apparent only from a long weak tail extending to lower wave numbers in both absorption and MCD spectra. Only in **1A** is there a very weak but distinct absorption maximum, located at 15,000 cm^{-1}. In all cases, the MCD of this very weak transition is extremely weak and negative (positive

B term). We have observed a similar weak peak at $\sim$16,000 cm^{-1} in the very air-sensitive 1,3,5-tri-*tert*-butylpentalene **1B,** of which we had only a slightly impure sample, so that we were not able to record reliably the higher energy region due to overlap with contributions from impurities.

The spectra contain a clear indication that an additional fairly intense band with a positive B term is present at 46,000–48,000 cm^{-1}. In **1A,** the absorption peak at $\sim$40,000 cm^{-1} has an MCD counterpart whose shape suggests that its B term is positive but that another transition with a negative B term is present at a slightly higher energy. In **2A,** the very different shapes of the absorption and MCD curves also suggest that such an additional transition may well be present.

PERIMETER MODEL

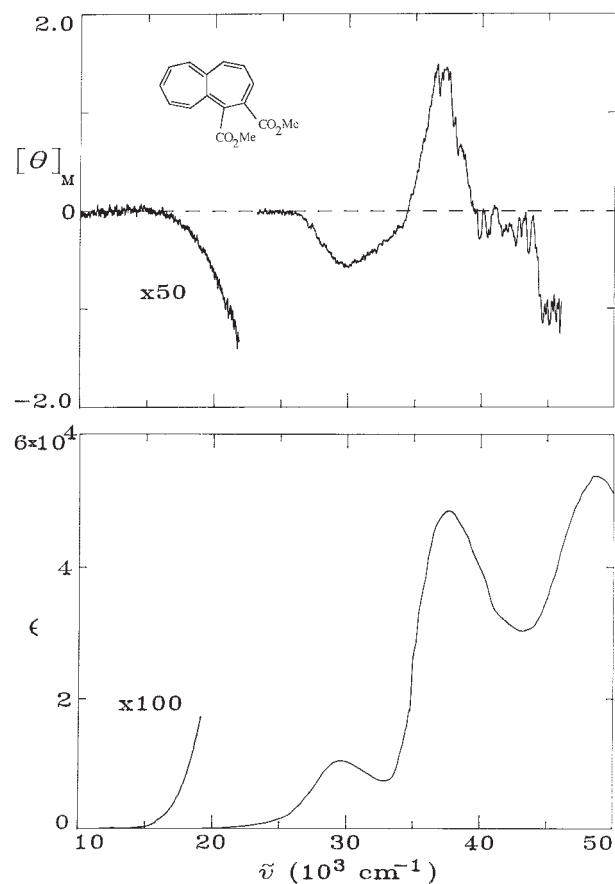The application of the simple perimeter model requires the knowledge of certain differences in

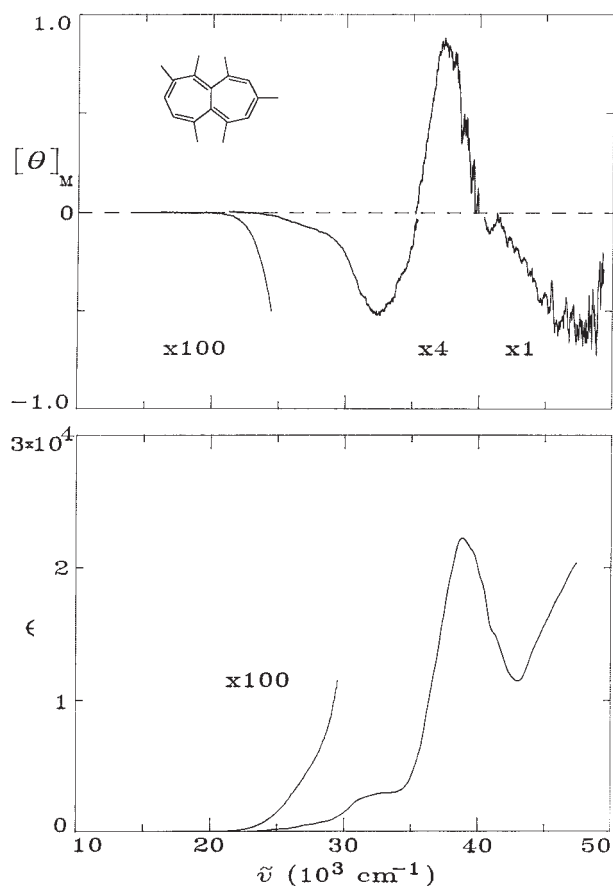**FIGURE 4.** Absorption (bottom) and MCD (top) of **2C** in cyclohexane.

FIGURE 5. Absorption (bottom) and MCD (top) of **2D** in cyclohexane.

and Table III for **2,** at both C_{2h} and D_{2h} geometries. Figures 6 and 7 provide the molecular orbital energy diagrams for the parent **1** and **2** and show the definitions of the quantities ΔH, ΔL, and ΔHSL. The first two of these are combined into a difference and a sum needed in the perimeter model; $\Delta HL = \Delta H - \Delta L$ and $\Sigma HL = \Delta H + \Delta L$. Table IV gives the energies of key configurations at the HF/TZVP level for both **1** and **2**. Configurations that are derived from the ground state Hartree–Fock (HF) determinant by single excitation from orbital x to orbital y are labeled Ψ_x^y (the symbols for the frontier orbitals involved are defined in Figs. 6 and 7). In the perimeter model, these excitations refer to perimeter molecular orbitals, and in numerical methods, they refer to the HF molecular orbitals. The energies of the HF-orbital based configurations (Table IV) fit the order anticipated on page 7769 of Part 3 of this series [11] for negative (**1**) and positive (**2**) ΔHSL, respectively.

CIS CALCULATIONS

The CIS $\pi\pi^*$ transition energies, intensities, and polarizations for **1** and **2,** along with the composition of excited state wavefunctions, are listed for both C_{2h} and D_{2h} geometries in Tables V and VI, respectively. Excited states are labeled by symbols provided by the perimeter model, because the composition of the wavefunctions is very close to that anticipated from this model. Some of the differences are undoubtedly due to the small difference between the perimeter and the HF molecular orbitals. The agreement is imperfect in case of the high-energy P_2 state. In **1** at C_{2h} symmetry, one of the single excitations contributing to the P_2 wavefunc-

molecular orbital energies and related quantities. These results were obtained at various levels of approximation and are collected in Table II for **1**

TABLE II
Computed orbital energy differences for pentalene[a] (eV).

	PMO[b]	HMO[b]	D$_{2h}$			C$_{2h}$		
			HF[c]	HF[d]	DFT[e]	HF[c]	HF[d]	DFT[e]
ΔHSL	−2	−0.940	−5.762	−6.863	−5.768	−6.004	−5.581	−5.092
ΔH	0.5	0.414	1.667	2.890	1.863	2.144	2.146	1.520
ΔL	0.5	0.586	2.394	2.045	2.187	2.223	1.935	1.979
ΔHL	0	−0.172	−0.727	0.845	−0.324	−0.079	0.211	−0.459
ΣHL	1	1	4.061	4.935	4.050	4.367	4.081	3.499

[a] At MP2/6-31+G* optimized geometry.
[b] In $|\beta|$ units.
[c] The DZP basis set.
[d] The TZVP basis set.
[e] The TZVP basis set and the B-P86 functional.

TABLE III
Computed orbital energy differences for heptalene[a] (eV).

	PMO[b]	HMO[b]	D$_{2h}$			C$_{2h}$		
			HF[c]	HF[d]	DFT[e]	HF[c]	HF[d]	DFT[e]
ΔHSL	1.333	1.240	4.562	4.629	2.822	3.534	3.604	2.396
ΔH	0.333	0.317	1.154	1.158	0.961	1.11	1.115	0.897
ΔL	0.333	0.295	2.908	2.889	1.932	2.21	2.203	1.660
ΔHL	0	0.022	−1.754	−1.731	−0.971	−1.1	−1.088	−0.763
ΣHL	0.667	0.612	4.062	4.047	2.893	3.32	3.318	2.557

[a] At MP2/6-31+G* optimized geometry.
[b] In $|\beta|$ units.
[c] The DZP basis set.
[d] The TZVP basis set.
[e] The TZVP basis set and the B-P86 functional.

FIGURE 6. The PMO derivation of the $\Delta HL = \Delta H - \Delta L$ and $\Delta HSL = 2(\Delta HS - \Delta LS)$ values for pentalene (A) and an interpretation of its electronic transitions (B); see text.
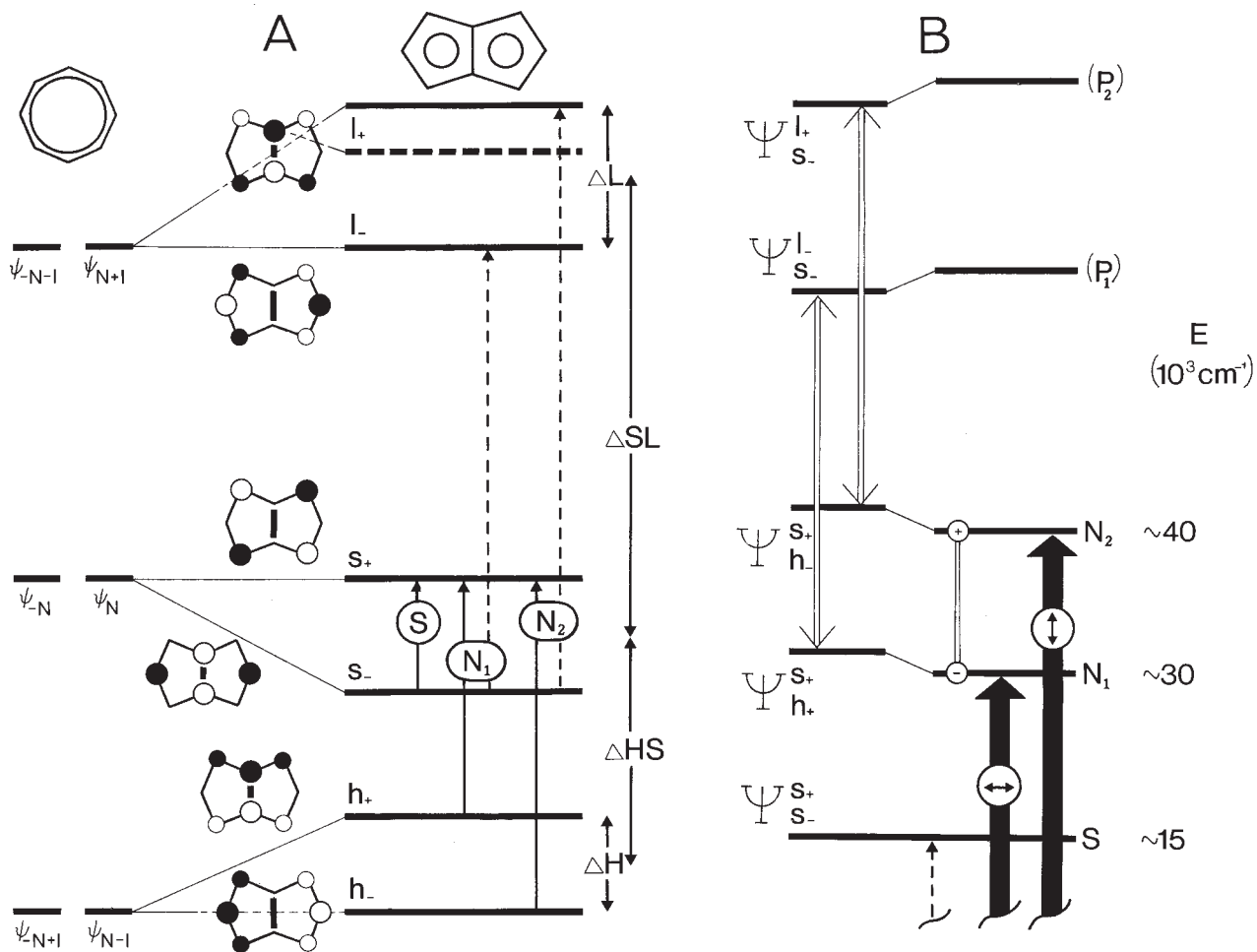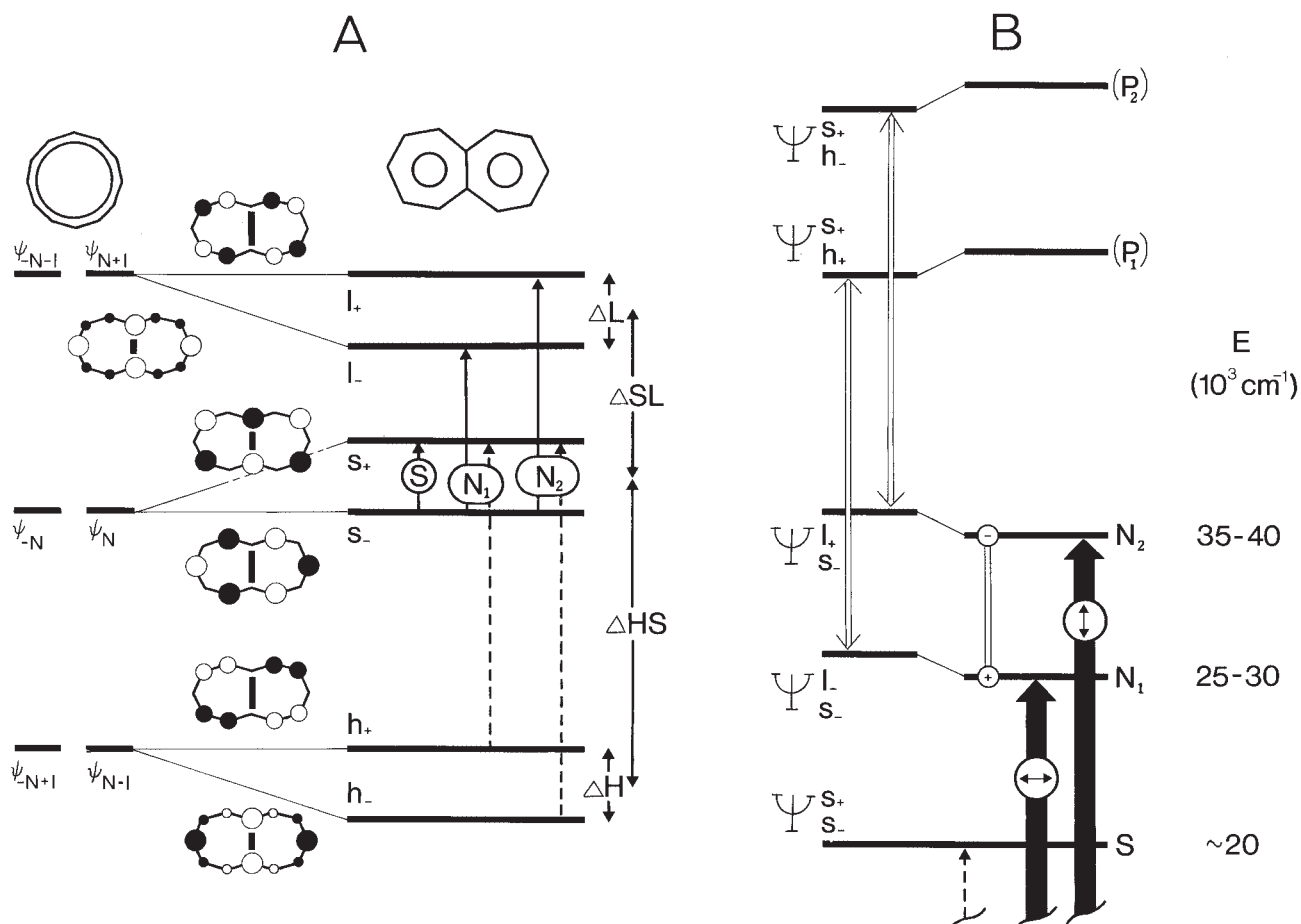
FIGURE 7. The PMO derivation of the $\Delta HL = \Delta H - \Delta L$ and $\Delta HSL = 2(\Delta HS - \Delta LS)$ values for heptalene (A) and an interpretation of its electronic transitions (B); see text.

tion involves an a_u "intruder" virtual orbital whose energy is shown as a dashed line in Figure 6. Similarly, in **2** at both symmetries, the P_2 wavefunction contains a contribution from a single excitation from an orbital whose energy is below those shown in Figure 7. At these high energies, we also find a forbidden transition to a state not contained in the

simple perimeter model (intruder state) and additional transitions to states of types other than $\pi\pi^*$.

DENSITY FUNCTIONAL CALCULATIONS

The TD-DFT electronic transition energies, intensities, and polarizations for **1** and **2,** along with the

TABLE IV _____

The CIS configuration energies (eV) of pentalene (1) and heptalene (2).

	1			2	
	D_{2h}	C_{2h}		D_{2h}	C_{2h}
Ψ_{h+}^{s+}	4.97	5.40	Ψ_{s-}^{l-}	3.71	4.09
Ψ_{h-}^{s+}	7.06	7.50	Ψ_{s-}^{l+}	5.98	6.47
Ψ_{s-}^{l-}	7.83	8.32	Ψ_{h+}^{s+}	6.06	6.46
Ψ_{s-}^{l+}	9.55	9.65	Ψ_{h-}^{s+}	7.27	7.53

TABLE V

The CIS results for low energy $\pi\pi^*$ states of pentalene (1).[a]

State[b]	D_{2h}					C_{2h}				
	Sym[c]	En[d]	Pol[c]	f^e	Contribution to state function (weight %)	Sym[c]	En[d]	Pol[c,f]	f^e	Contribution to state function (weight %)
S	$1B_{1g}$	6.3	—	0	Ψ_{s-}^{s+} (98.0)	$2A_g$	16.9	—	0	Ψ_{s-}^{s+} (97.7)
N_1	$1B_{3u}$	30.6	x	0.37	Ψ_{h+}^{s+} (92.0), Ψ_{s-}^{l-} (4.4)	$1B_u$	35.6	8	0.25	Ψ_{h+}^{s+} (90.7), Ψ_{s-}^{l-} (3.6), Ψ_{s-}^{s+} (2.3)
N_2	$1B_{2u}$	50.1	y	0.33	Ψ_{h-}^{s-} (94.5)	$2B_u$	54.6	−46	0.32	Ψ_{h+}^{s+} (90.1), Ψ_{s-}^{l-} (4.0)
P_1	$2B_{3u}$	58.1	x	1.27	Ψ_{s-}^{l-} (89.3), Ψ_{h+}^{s} (3.6)	$3B_u$	62.2	−26	1.31	Ψ_{s-}^{l-} (85.4), Ψ_{h+}^{s} (4.4), Ψ_{h-}^{s} (2.6)
—						$3A_g$	66.9	—	0	Ψ_{h+}^{l-} (79.7)
P_2						$4B_u$	71.9	8	0.27	Ψ_{s-}^{l+} (79.1), Ψ_{h+}^{au} (1.5)

[a] At MP2/6-31+G* optimized geometries.
[b] Perimeter state label.
[c] Long axis: x, short axis: y, out-of-plane axis: z.
[d] Energy in 10^3 cm^{-1}.
[e] Dipole length formula for oscillator strength.
[f] Angle in degrees, measured counterclockwise from the horizontal axis in formula **1**.

squares of amplitudes of the contributing single excitations, are listed for both C_{2h} and D_{2h} geometries in Tables VII and VIII, respectively. The results for the nature of the excitations, state symmetries, and transition polarizations correspond closely to those obtained at the CIS level, but the excitation energies are somewhat different. The nature of the low-energy excitations is that anticipated from the perimeter model. Now, a larger number of intruder states of $\pi\pi^*$ type and others is predicted at higher energies; again, only $\pi\pi^*$ excitations are listed.

SACCI CALCULATIONS

The SACCI $\pi\pi^*$ transition energies, intensities, and polarizations for **1** and **2,** along with the composition of excited state wavefunctions, are listed for both C_{2h} geometries in Tables IX and X, respectively. They correspond closely to the CIS and TD-DFT results and to the expectations based on the perimeter model. An even larger number of intruder states is predicted at higher energies. Tables IX and X also list the B term for each transition into excited state F, calculated as a sum over two con-

TABLE VI

The CIS results for low energy $\pi\pi^*$ states of heptalene (2).[a]

State[b]	D_{2h}					C_{2h}				
	Sym[c]	En[d]	Pol[c]	f^e	Contribution to state function (weight %)	Sym[c]	En[d]	Pol[c,f]	f^e	Contribution to state function (weight %)
S	$1B_{1g}$	6.3	—	0	Ψ_{s-}^{s+} (97.4)	$2A_g$	14.7	—	0	Ψ_{s-}^{s+} (96.7)
N_1	$1B_{3u}$	22.2	x	0.48	Ψ_{s-}^{l-} (89.1), Ψ_{h+}^{s+} (7.3)	$1B_u$	26.5	8	0.29	Ψ_{s-}^{l-} (87.7), Ψ_{h+}^{s+} (6.8), Ψ_{s-}^{l+} (2.3)
N_2	$1B_{2u}$	42.0	y	0.30	Ψ_{s-}^{l+} (85.0), Ψ_{b3g}^{l-} (9.6), Ψ_{s-}^{s+} (2.6)	$2B_u$	47.1	−75	0.10	Ψ_{s-}^{l+} (73.1), Ψ_{h+}^{s+} (15.4), Ψ_{s-}^{s+} (4.0)
P_1	$2B_{3u}$	45.4	x	1.96	Ψ_{h+}^{s+} (86.3), Ψ_{s-}^{l-} (6.3)	$3B_u$	48.8	−24	2.05	Ψ_{h+}^{s+} (70.5), Ψ_{s-}^{l+} (13.7), Ψ_{s-}^{l-} (8.4)
—	$2B_{1g}$	46.5	—	0	Ψ_{h+}^{l-} (93.7)	$3A_g$	51.9	—	0	Ψ_{h+}^{l-} (88.4), Ψ_{bg}^{s} (6.3)
P_2	$2B_{2u}$	50.4	y	0.03	Ψ_{h+}^{s+} (72.1), Ψ_{b3g}^{l-} (14.7), Ψ_{s-}^{l+} (7.8)	$4B_u$	54.5	21	0.57	Ψ_{h-}^{s+} (80.6), Ψ_{bg}^{l-} (5.8), Ψ_{s-}^{l+} (4.8)

[a] At MP2/6-31+G* optimized geometries.
[b] Perimeter state label.
[c] Long axis: x, short axis: y, out-of-plane axis: z.
[d] Energy in 10^3 cm^{-1}.
[e] Dipole length formula for oscillator strength.
[f] Angle in degrees, measured counterclockwise from the horizontal axis in formula **2**.

TABLE VII
The TD-DFT results for low energy $\pi\pi^*$ states of pentalene (1).[a]

| State[b] | D_{2h} | | | | | | C_{2h} | | | | | |
	Sym[c]	En[d]	Pol[c]	f[e]	Transition	Weight (%)	Sym[c]	En[d]	Pol[c,f]	f[e]	Transition	Weight (%)
S	$1B_{1g}$	3.5	—	0	$s_- \to s_+$	(99.9)	$2A_g$	11.6	—	0	$s_- \to s_+$	(99.9)
N_1	$1B_{3u}$	26.7	x	0.14	$h_+ \to s_+$	(93.8)	$1B_u$	29.1	9	0.10	$h_+ \to s_+$	(93.9)
N_2	$1B_{2u}$	38.3	y	0.10	$h_- \to s_+$	(94.1)	$2B_u$	38.8	−66	0.03	$h_- \to s_+$	(72.8)
											$s_- \to l_-$	(25.0)
P_1	$2B_{3u}$	47.4	x	0.70	$s_- \to l_-$	(92.6)	$3B_u$	51.3	−21	0.66	$s_- \to l_-$	(69.3)
											$h_- \to s_+$	(19.2)
											$h_+ \to 4a_u$	(4.7)
—	$2B_{1g}$	51.2	—	0	$1b_{1u} \to s_+$	(52.8)	$3A_g$	52.2	—	0	$s_- \to 4a_u$	(65.1)
					$h_+ \to l_-$	(47.1)					$1a_u \to s_+$	(32.6)
—	$2A_g$	51.8	—	0	$s_- \to 3b_{1u}$	(95.7)	$4A_g$	55.0	—	0	$h_+ \to l_-$	(72.7)
											$s_- \to 4a_u$	(14.0)
											$1a_u \to s_+$	(11.7)
—	$3B_{1g}$	57.7	—	0	$h_+ \to l_-$	(51.6)	$5A_g$	60.8	—	0	$1a_u \to s_+$	(49.3)
					$1b_{1u} \to s_+$	(45.5)					$h_+ \to l_-$	(23.6)
											$s_- \to 4a_u$	(15.5)
											$h_+ \to l_+$	(5.1)
P_2	$2B_{2u}$	60.2	y	0.01	$s_- \to l_+$	(71.6)	$4B_u$	61.3	18	0.23	$s_- \to l_+$	(90.3)
					$h_+ \to 3b_{1u}$	(26.9)						

[a] At MP2/6-31+G* optimized geometries.
[b] Perimeter state label.
[c] Long axis: x, short axis: y, out-of-plane axis: z.
[d] Energy in 10^3 cm^{-1}.
[e] Dipole length formula for oscillator strength.
[f] Angle in degrees, measured counterclockwise from the horizontal axis in formula **1**.

tributions from each of the lowest 32 states I [26]. One of these, $B^F_{I,G}$, is due to the magnetic mixing of the I-th state into the ground state, and the other, $B^F_{I,F}$, is due to the magnetic mixing of the I-th state into the final state F. In Tables XI and XII, we list the values of these contributions for the lowest few excited states of **1** and **2,** respectively. The contribution ordinarily also present from the mutual mixing of the ground and final states, $B^F_{G,F} + B^F_{F,G}$, vanishes for centrosymmetric molecules, because it is proportional to the difference of ground and excited state dipole moments. It is neglected in the simple perimeter model [11].

Discussion

THE STRUCTURE OF 1 AND 2

The solution geometries of the pentalenes and heptalenes under investigation here are not known, but our and prior [5, 27] calculations for the isolated molecules agree that single and double bonds alternate in both **1** and **2**. In a crystal [28], **1A** is planar with localized double bonds, and **1B** is planar, as well. The crystal structure of **2C** is nonplanar, the two seven-membered rings forming a boat conformation with double-bond localization [29]. In the less hindered **2B,** the boat conformation is more nearly planar and the double bond alternation, less extreme [30]. In solution, rapid interconversion between the two valence tautomers differing by double bond location occurs very fast at room temperature, particularly in the symmetrically substituted derivatives [9, 31], in the planar ones possibly by heavy atom tunneling in analogy to the behavior of cyclobutadiene [32]. This is unlikely to be fast on the UV time scale and can be ignored for the current purposes. Some of the derivatives of **2** are undoubtedly quite severely nonplanar, in particular **2D.** This is very likely the reason for the overall blue shift of its transitions. Still, its general spectral pattern is not different from the others, and the MCD sign pattern is the same.

TABLE VIII

The TD-DFT results for low energy $\pi\pi^*$ states of heptalene (2).[a]

State[b]	D_{2h}						C_{2h}					
	Sym[c]	En[d]	Pol[c]	f^e	Transition	Weight (%)	Sym[c]	En[d]	Pol[c,f]	f^e	Transition	Weight (%)
S	$1B_{1g}$	3.8	—	0	$s_- \to s_+$	(100.0)	$2A_g$	8.4	—	0	$s_- \to s_+$	(100.0)
N_1	$1B_{3u}$	19.0	x	0.16	$s_- \to l_-$	(89.3)	$1B_u$	20.7	4	0.13	$s_- \to l_-$	(90.9)
					$h_+ \to s_+$	(10.1)						
N_2	$1B_{2u}$	31.3	y	0.05	$s_- \to l_+$	(87.8)	$2B_u$	30.7	27	0.02	$s_- \to l_+$	(52.5)
					$h_- \to s_+$	(8.1)					$h_+ \to s_+$	(45.5)
P_1	$2B_{3u}$	35.2	x	0.88	$h_+ \to s_+$	(87.9)	$3B_u$	38.9	−24	0.76	$h_+ \to s_+$	(43.1)
					$s_- \to l_-$	(9.1)					$s_- \to l_+$	(37.8)
											$2b_g \to l_-$	(9.5)
—	$2B_{1g}$	37.4	—	0	$h_+ \to l_-$	(95.8)	$3A_g$	38.9	—	0	$h_+ \to l_-$	(92.1)
P_2	$2B_{2u}$	40.2	y	0.11	$h_- \to s_+$	(78.5)	$4B_u$	41.0	19	0.40	$h_- \to s_+$	(87.8)
					$1b_{3g} \to l_-$	(17.3)					$h_+ \to s_+$	(3.1)
—	$2A_g$	40.3	—	0	$1b_{3g} \to s_+$	(83.1)	$4A_g$	42.3	—	0	$2b_g \to s_+$	(80.3)
					$h_- \to l_-$	(14.5)					$h_- \to l_-$	(12.2)
—	$3A_g$	46.6	—	0	$h_- \to l_-$	(70.5)	$5A_g$	47.7	—	0	$h_- \to l_-$	(72.7)
					$s_- \to 3b_{2g}$	(16.6)					$s_- \to 5b_g$	(10.9)
					$1b_{3g} \to s_+$	(8.5)					$2b_g \to s_+$	(7.2)

[a] At MP2/6-31+G* optimized geometries.
[b] Perimeter state label.
[c] Long axis: x, short axis: y, out-of-plane axis: z.
[d] Energy in 10^3 cm^{-1}.
[e] Dipole length formula for oscillator strength.
[f] Angle in degrees, measured counterclockwise from the horizontal axis in formula **2**.

TABLE IX

The SACCI results for low energy $\pi\pi^*$ states of C_{2h} pentalene (1).[a]

State[b]	Sym	En[c]	Pol[d]	f^e	B^f	Contribution to state function (weight %)
S	$2A_g$	14.4	—	0	—	Ψ^{s+}_{s-} (88.4), $\Psi^{s+\,s+}_{s-\,s-}$ (2.6)
N_1	$1B_u$	32.6	9	0.13	−0.09	Ψ^{s+}_{h+} (77.4), Ψ^{s+}_{h-} (6.8)
N_2	$2B_u$	42.2	−42	0.09	−0.24	Ψ^{s+}_{h-} (51.8), $\Psi^{s+\,s+}_{s-\,h+}$ (17.6), Ψ^{l-}_{s-} (14.4), Ψ^{s+}_{h+} (5.8)
D	$3A_g$	46.3	—	0.00	0.00	$\Psi^{s+\,s+}_{s-\,s-}$ (72.3), $\Psi^{l-\,s+}_{s-\,h-}$ (5.3)
—	$4A_g$	53.6	—	0.00	0.00	Ψ^{s+}_{au} (42.3), $\Psi^{s+\,s+}_{h+\,h-}$ (30.3), Ψ^{au}_{s-} (16.0)
P_1	$3B_u$	58.1	−22	1.00	0.83	Ψ^{l-}_{s-} (67.2), Ψ^{s+}_{h-} (8.4)
—	$5A_g$	64.8	—	0.00	0.00	Ψ^{l-}_{h+} (47.6), $\Psi^{s+\,s+}_{h+\,h+}$ (10.2), Ψ^{s+}_{au} (9.6)
—	$6A_g$	72.2	—	0.00	0.00	$\Psi^{s+\,s+}_{h+\,h+}$ (43.6), Ψ^{au}_{s-} (28.1), $\Psi^{s+\,s+}_{h+\,h-}$ (6.8)
—	$4B_u$	76.7	−74	0.79	0.07	Ψ^{au}_{h+} (67.2), $\Psi^{l-\,s+}_{s-\,s-}$ (8.4)
P_2	$5B_u$	77.9	29	0.22	−0.08	$\Psi^{s+\,s+}_{s-\,h-}$ (41.0), $\Psi^{l-\,s+}_{s-\,s-}$ (37.2), Ψ^{l+}_{s-} (29.2)

[a] At MP2/6-31+G* optimized geometry. Long axis: x, short axis: y, out-of-plane axis: z.
[b] Perimeter state label.
[c] Energy in 10^3 cm^{-1}.
[d] Angle in degrees, measured counterclockwise from the horizontal axis in formula **1**.
[e] Dipole length formula for oscillator strength.
[f] B term in 10^{-3} Bohr magneton Debye^2/cm^{-1}.

TABLE X

The SACCI results for low energy $\pi\pi^*$ states of C_{2h} heptalene (2).[a]

State[b]	Sym	En[c]	Pol[d]	f[e]	B[f]	Contribution to state function (weight %)
S	$2A_g$	12.9	—	0.00	0.00	Ψ^{s+}_{s-} (84.6), $\Psi^{s+\ s+}_{s-\ s-}$ (2.6)
N_1	$1B_u$	25.1	3	0.17	0.56	Ψ^{l-}_{s-} (79.2), Ψ^{s+}_{h+} (4.0), Ψ^{l+}_{s-} (3.6)
N_2	$2B_u$	35.4	−71	0.01	0.20	Ψ^{l+}_{s-} (39.7), $\Psi^{l-\ s+}_{s-\ s-}$ (28.1), Ψ^{s+}_{h+} (23.0).
—	$3A_g$	44.3	—	0	0	Ψ^{l-}_{h+} (53.3), $\Psi^{s+\ s+}_{s-\ s-}$ (9.6), Ψ^{s+}_{bg} (7.8)
—	$4A_g$	44.7	—	0	0	Ψ^{s+}_{bg} (21.2), $\Psi^{l-\ l-}_{s-\ s-}$ (19.4), Ψ^{l-}_{h-} (16.0), Ψ^{l-}_{h+} (13.7)
P_1	$3B_u$	45.8	−14	1.24	−3.54	Ψ^{s+}_{h+} (49.0), Ψ^{l-}_{s-} (9.6), $\Psi^{l-\ s+}_{s-\ s-}$ (9.0)
P_2	$4B_u$	46.0	70	0.17	2.96	Ψ^{s+}_{h+} (53.3), Ψ^{l+}_{s-} (8.4), Ψ^{l-}_{bg} (6.8)
—	$5B_u$	54.8	−20	0.51	0.49	Ψ^{s+}_{s-} (22.1), Ψ^{l-}_{bg} (20.3), $\Psi^{bg-}_{s-\ s-}$ (8.4)

[a] At MP2/6-31+G* optimized geometry. Long axis: x, short axis: y, out-of-plane axis: z.
[b] Perimeter state label.
[c] Energy in 10^3 cm^{-1}.
[d] Angle in degrees, measured counterclockwise from the horizontal axis in formula **2**.
[e] Dipole length formula for oscillator strength.
[f] B term in 10^{-3} Bohr magneton Debye^2/cm^{-1}.

The application of the perimeter model to the interpretation of the absorption and MCD spectra tolerates deviations from planarity and other perturbations, particularly for hard chromophores whose MCD signs are insensitive to perturbations. After all, deviation from planarity and introduction of nonuniform bond lengths are relatively minor perturbations compared with the main one, the introduction of a cross-link into the perimeter. In the following general analysis of the principal features, we concentrate on the essentials and leave the geometrical effects aside, assuming that the molecules are of C_{2h} or D_{2h} symmetry.

ORBITAL ENERGY DIFFERENCES

We use perturbation theory at the Hückel level (PMO [33] theory) to deduce the orbital energy differences pertinent to spectral interpretations.

Both **1** and **2** are derived from uncharged perimeters by introduction of a single cross-link between atoms whose indices add up to an even number (0 and 4 in the [8] annulene perimeter for **1**, 0 and 6 in the [12] annulene perimeter for **2**). The cross-link therefore represents an even perturbation in the sense of Moffitt [34].

The even nature of the perimeter perturbation that produces **1** and **2** distinguishes these π systems fundamentally from their analogues, benzocyclobutadiene and biphenylene, in making them nonalternant. As a result, nonvanishing values for the critical orbital energy differences can and do result already in the PMO, Hückel, or Pariser, Parr, and Pople (PPP) approximations, permitting back-of-the-envelope MCD sign predictions. In contrast, it is much more difficult to predict correctly the relative magnitude of ΔHL and ΔHSL and the negative sign of the former for biphenylene [1].

TABLE XI

Analysis of state-mixing contributions to the B terms of pentalene (C_{2h}).[a]

State F	B	$B^F_{S,\,G}$	$B^F_{N_1,F}$	$B^F_{N_2,F}$	$B^F_{P_1,F}$	$B^F_{P_2,F}$	$B^F_{4B_u,F}$
N_1	−0.09	−0.046	—	−0.033	−0.054	0	0.050
N_2	−0.24	−0.266	0.033	—	−0.005	0.013	0.006
P_1	0.83	0.345	0.054	0.005	—	0.308	0.038
P_2	−0.08	0.398	0	−0.013	−0.308	—	−0.140
$4B_u$	0.07	−0.061	−0.050	−0.006	−0.038	0.140	—

[a] SACCI, active space 20/50 [25].

TABLE XII

Analysis of state-mixing contributions to the B terms of heptalene (C_{2h}).[a]

State F	B	$B_{S,G}^F$	$B_{N_1,F}^F$	$B_{N_2,F}^F$	$B_{P_1,F}^F$	$B_{P_2,F}^F$	$B_{5Bu,F}^F$
N_1	0.56	0.321	—	0.020	0.016	0.129	0.045
N_2	0.20	0.157	−0.020	—	0.002	0.008	0.027
P_1	−3.54	−0.742	−0.016	−0.002	—	−3.232	−0.009
P_2	2.96	−0.148	−0.129	−0.008	3.232	—	0.135
$5B_u$	0.49	0.409	−0.045	−0.027	0.009	−0.135	—

[a] SACCI, active space 20/50 [25].

A simple derivation of the ΔHL and ΔHSL values for **1** and **2** is shown in Figures 6(A) and 7(A). These show the real form of the Hückel orbitals and their energies in the parent perimeters and indicate how the cross-linking perturbation splits them into the orbitals of **1** and **2**. The HO (highest doubly occupied), SO (singly occupied), and LU (lowest unoccupied) orbital pairs are of particular significance for the perimeter model. Because one of the members of each pair has a node at both atoms that are being linked, its energy is not affected in the first approximation. The nodal properties of the perimeter orbitals make it clear that the other member of each pair is affected very strongly, in a regular fashion: the nonbonding orbital is stabilized in **1** and destabilized in **2,** whereas the active members of the HO and LU pairs move in the opposite directions. As a result, in **1** the average energy of s_- and s_+ is quite close to the average energy of h_- and h_+ and quite far from that of l_- and l_+, such that $\Delta HSL = 2(\Delta HS - \Delta LS) \ll 0$. In **2**, the exact opposite is true, and $\Delta HSL \gg 0$. This mirror-image–like behavior of **1** and **2** is clearly due to the same factors that cause other approximately mirror-image types of behavior, such as the tendency of **1** to acquire two negative charges and the tendency of **2** to acquire two positive charges, etc.

To first order of perturbation theory, in both **1** and **2,** the orbital splitting ΔH and ΔL should be equal ($0.5|\beta|$ in **1** and $0.33|\beta|$ in **2**), leading to a vanishing $\Delta HL = \Delta H - \Delta L$. The actual Hückel values are indeed approximately equal and ΔHL values are small (Tables II and III). In contrast, both the PMO and the Hückel ΔHSL values are large and are strongly negative in **1** and strongly positive in **2.** The same result is obtained from HF and DFT orbital energies (Tables II and III).

Clearly, both simple considerations and advanced calculations agree that both **1** and **2** are orbital-shift–dominated [11] MCD chromophores ($|\Delta HSL| > \Sigma HL > |\Delta HL|$) [35] and that **1** is negative-hard ($\Delta HSL < 0$), whereas **2** is positive-hard ($\Delta HSL > 0$) [11]. Now, qualitative predictions of spectroscopic properties from the perimeter model follow automatically, and perturbations by substituents, bond length alternation, or nonplanarity are not likely to affect them.

PERIMETER MODEL PREDICTIONS

Perimeter model predictions are depicted in Figures 6 and 7 [2, 10–12]. Taking either of the two planes of symmetry perpendicular to the molecular plane at the D_{2h} geometry, which we consider first in this simple approximation, we note that the symmetries of the molecular orbitals h_- and l_- are the same. It follows that the perturbations that produce **1** and **2** from their respective perimeters are of the C type [11, 12] and the results given in Table II and Figure 3 of Part 3 [11] apply. In order to deduce the signs of contributions to MCD B terms expected in the perimeter model from the mutual magnetic mixing of excited states, which is ordinarily sufficient, we need only use the orbital energy differences ΔH, ΔL, and ΔHSL. Going to the actual C_{2h} equilibrium geometry of the ground state is a minor perturbation on this scale and is not expected to change the MCD sign predictions. However, we note that for **1** and **2** the orbital energy splitting ΔS is unusually small and that there is a good chance that the contributions due to the magnetic mixing of the S state to the ground state, whose magnitudes are also predicted by the perimeter model, cannot be ignored and may actually dominate. Indeed, these contributions alone would predict the signs observed. It would be difficult to rely on this observation by itself and claim that this proves that the magnetic mixing of the ground state with the S state indeed determines the MCD signs, but the

SACCI calculations discussed below lead to the same conclusion.

Figures 6(B) and 7(B) show the expected ordering of configuration energies (cf. the left side of Figure 2 in Part 3 [11]). For **1**, Ψ_{h+}^{s+} is lowest, Ψ_{h-}^{s+} is considerably higher (roughly by ΔH), and $\Psi_{s-}^{\ell-}$ and $\Psi_{s-}^{\ell+}$ are very much higher still. For **2,** $\Psi_{s-}^{\ell-}$ is lowest, with $\Psi_{s-}^{\ell+}$ higher by roughly ΔL, and Ψ_{h+}^{s+} and Ψ_{h-}^{s+}, much higher. The anticipation is fully confirmed by numerical calculations at the CIS level, which give similar results at D_{2h} and C_{2h} geometries (Table IV). From the configuration energies listed in Table IV and the Eqs. (20) in Part 3 [11] we obtain (in eV) for **1** $\Delta L = 1.72$, $\Delta H = 2.09$, and $\Delta HSL = -5.35$ at D_{2h} symmetry and $\Delta L = 1.33$, $\Delta H = 2.10$, and $\Delta HSL = -5.08$ at C_{2h} symmetry. For **2,** we get $\Delta L = 2.27$, $\Delta H = 1.20$, and $\Delta HSL = 3.64$ at D_{2h} symmetry and $\Delta L = 2.38$, $\Delta H = 1.07$, and $\Delta HSL = 3.44$ at C_{2h} symmetry. These numbers agree qualitatively with the numbers listed in Table III, which were obtained from HF or Kohn–Sham orbital energies.

Because of the large energy difference between the HO $\rightarrow$ SO and the SO $\rightarrow$ LU excitations in both **1** and **2,** the effects of configuration interaction within this 4×4 subspace (expression (17) in Part 3 [11]) will be small. The spectroscopic properties expected from the simple arguments are also briefly summarized in Figures 6(B) and 7(B). Tables V and VI (CIS, D_{2h}, and C_{2h}), VII and VIII (TD-DFT, D_{2h}, and C_{2h}), and IX and X (SACCI and C_{2h} only) show that the qualitative expectations concerning the nature of the wavefunctions deduced from the perimeter model are entirely confirmed by numerical calculations and that the results are qualitatively similar at D_{2h} and C_{2h} geometries.

At D_{2h} geometry, the 3×3 configuration interaction matrix from which the G, S, and D states result (expression (16) in Part 3 [11]) is already diagonal for an even perturbation of the perimeter, because the phase angle σ equals 0 or π ($\sigma = \pi$ in **1** and $\sigma = 0$ in **2**). The question then is whether the closed-shell configuration Ψ_R or the open-shell configuration Ψ_{s-}^{s+} represents the ground state. The former is the case if the perturbation is large enough and $\Delta S > 2[2N]$, where ΔS is the $S_- - S_+$ orbital energy difference, and $[2N]$ is an electron repulsion integral defined in Eq. (10) of Part 1 [2], compare Eq. (20) in Part 3 [11]. We refer to such molecules as "unaromatic." The latter would be the case in the largely hypothetical more weakly perturbed truly "antiaromatic" perimeters, discussed only in Part 1 [2]. The state-crossing point of exact degeneracy of the Ψ_R and Ψ_{s-}^{s+} states (critically het-

erosymmetric biradicaloid [36]) corresponds to the conical intersection first identified in **1** in CCI calculations at the PPP level [37]. At the optimized D_{2h} and C_{2h} geometries, the CIS and DFT calculations yield Ψ_R as the ground state by a small margin and Ψ_{s-}^{s+} as the first excited singlet state (Tables V–VIII), as does the SACCI calculation for the C_{2h} geometry (Tables IX and X). At the optimized D_{2h} geometry SACCI yields Ψ_{s-}^{s+} as the ground state for **1** and **2**, and a more elaborate computation would be necessary to verify whether this is really correct.

At C_{2h} geometries, to which the experimental data refer, σ is no longer constrained and the 3×3 CI matrix from which the G, S, and D states result is no longer diagonal. Now, all three methods of calculation, CIS, TD-DFT, and SACCI yield totally symmetric closed-shell ground states, in agreement with experiment for both **1** and **2.** These are used below for spectral interpretations, which are based on a combination of the perimeter model and all three types of calculations, all of which agree for the low-energy states. Prior complete active space–self-consistent field (CAS-SCF) and complete active space–second-order perturbation theory (CASPT2) calculations [5] were performed for **1** and at C_{2h} symmetry, and their results are in good agreement with ours.

STATE ASSIGNMENTS

We propose that the transition to the S state, predicted to have a vanishing absorption and MCD intensity, is responsible for the weak low-energy band observed in the spectra of **1A** and **1B** and for the weak low-energy tail observed for **2A–D.** We attribute the shape to a combination of intensity borrowing by vibronic coupling and of Franck–Condon forbiddenness (the bond length alternation should be absent or strongly reduced in the S state). The strongly forbidden G $\rightarrow$ D transition is apparently not observed.

Following prior work [5], the fairly intense band at 25,000–35,000 cm^{-1} is assigned as a superposition of the G $\rightarrow$ N$_1$ and G $\rightarrow$ N$_2$ transitions. At D_{2h} geometries, the former should be polarized across the cross-linking bond, the latter parallel to it [cf. the nodal properties of the molecular orbitals shown in Figs. 6(A) and 7(A)]. At C_{2h} geometries, these polarization directions are only approximately as stated (Tables V–X). The high strength of the transitions, compared with, say, the G $\rightarrow$ N$_1$ and G $\rightarrow$ N$_2$ transitions in biphenylene [1], is a result of the small degree of configuration mixing in

the 4×4 submatrix, which would transfer intensity to the P states [11]. The apparently higher intensity of the short-axis polarized $G \rightarrow N_2$ band at higher energy, observed despite the geometrical deformation of the perimeter from the ideal regular polygon shape, which favors transition moments directed along the long axis, indicates that the Ψ_{h+}^{s+}–$\Psi_{s-}^{\ell-}$ mixing is stronger than the Ψ_{h-}^{s+}–$\Psi_{s-}^{\ell+}$ mixing, that is, that ΔHL is somewhat negative for **1** and positive for **2,** as is calculated even at the Hückel level.

The P_1 state is assigned to the intense band at $35{,}000$–$40{,}000$ cm^{-1}. The P_2 state is expected to lie at much higher energies and probably is not observed in our spectra. We doubt that the results of the simple perimeter model are meaningful for such high-energy states, primarily because of the expected strong mixing with configurations ignored in the model. However, the numerical computations are still crude enough that we hesitate to attempt an assignment for the band observed in our spectra at $45{,}000$–$50{,}000$ cm^{-1}.

MAGNETIC CIRCULAR DICHROISM

Because of the relative proximity of the observed N_1 and N_2 states and their large separation from the P_1 and P_2 states, one might have expected the B terms of the $G \rightarrow N_1$ and $G \rightarrow N_2$ transitions to be dominated by the N_1–N_2 magnetic mixing. From the perimeter model, for $\Delta HSL < 0$, as in **1,** they should be $N_1 : -$, $N_2 : +$, and for $\Delta HSL > 0$, as in **2,** they should be $N_1 : +$, $N_2 : -$. However, because the excitation energy of the S state is very small, the magnetic mixing of the S state into the ground state is expected to have a large effect and could well dominate. According to Table II in Part 3 [11], it should make negative contributions to the B terms of both transitions in **1** and positive ones in **2.** Their effect is to greatly reinforce the first B term and invert the sign of the second. Because this produces the observed sign for the latter in the derivatives of both **1** and **2,** we conclude that the mixing of the ground state with the S state indeed dominates. Because ΔHSL in both compounds is so large, substitution should have a negligible chance to reverse its sign. The term resulting from the magnetic mixing with the ground state is insensitive to substitution, and the MCD sign patterns should be the same for all derivatives. All of this is exactly as observed.

An alternative interpretation of the observed signs of the B term of the N_2 transition would be to claim that the magnetic mixing of the ground with the S state does not dominate, but the perimeter model fails for this state. It is therefore of critical importance that we can verify the perimeter model predictions regarding the signs of contributions of various types of magnetically induced state mixing by SACCI calculations. Unlike the total magnitudes of B terms, these are not available from experiment. As is seen in Tables XI and XII, the individual SACCI contributions from the magnetic mixing of states are in perfect agreement with those deduced from the perimeter model, and it appears highly unlikely that this is a coincidence. The sign of the B term of the N_2 transition calculated at the SACCI level is clearly dominated by the contribution provided by the mixing of the ground and S states.

Conclusions

The $4N$-electron perimeter version of the perimeter model provides an intuitively satisfying qualitative rendition of the gross features of the absorption and MCD spectra of pentalenes and heptalenes, including simple a priori predictions of MCD signs and correlations of states with those of related classes of compounds. However, like its classical $(4N + 2)$-electron counterpart, in itself it is not sufficient for a detailed analysis of the electronic states of any one compound.

From a combination of arguments based on the simple perimeter model and numerical calculations, we conclude that the MCD signs of the derivatives of pentalene and heptalene that we studied, and presumably all others, are dominated by magnetic mixing of the ground with the first excited state. To our knowledge, this situation has not been observed before for an organic molecule.

ACKNOWLEDGMENT

References

1. Fleischhauer, J.; Höweler, U.; Spanget-Larsen, J.; Raabe, G.; Michl, J. (Part 5). J Phys Chem 2004, 108, 3225.

2. Höweler, U.; Downing, J. W.; Fleischhauer, J.; Michl, J. Perkin Transactions 1998, 2, 1101.

3. Baird, N. C.; West, R. M. J Am Chem Soc 1971, 93, 3072; Nakajima, T. Fortsch Chem Forsch 1972, 32, 1.

4. Falchi, A.; Gellini, C.; Salvi, P. R.; Hafner, K. J Phys Chem 1995, 99, 14659.

5. Bally, T.; Chai, S.; Neuenschwander, M.; Zhu, Z. J Am Chem Soc 1997, 119, 1869.

6. Falchi, A.; Gellini, C.; Salvi, P. R.; Hafner, K. J Phys Chem A 1998, 102, 5006.

7. Dauben, H. J.; Bertelli, D. J. J Am Chem Soc 1961, 83, 4659.

8. Le Goff, E. J Am Chem Soc 1962, 84, 3975; Hafner, K. Pure Appl Chem Suppl 2, 1971, 1; Hafner, K.; Dönges, R.; Goedecke, E.; Kaiser, R. Angew Chem Int Ed Engl 1973, 12, 337; Bloch, R.; Marty, R. A.; de Mayo, P. J Am Chem Soc 1971, 93, 3071; Bull Soc Chim Fr 1972, 203.

9. Hafner, K.; Süss, H. U. Angew Chem Int Ed Engl 1973, 12, 575.

10. Fleischhauer, J.; Höweler, U.; Michl, J. Spectrochim Acta 1999, 55A, 585.

11. Fleischhauer, J.; Höweler, U.; Michl, J. J Phys Chem A 2000, 104, 7762.

12. Fleischhauer, J.; Michl, J. J Phys Chem A 2000, 104, 7776.

13. Hafner, K.; Suda, M. Angew Chem Int Ed Engl 1976, 15, 314.

14. Vogel, E.; Ippen, J. Angew Chem Int Ed Engl 1974, 13, 734.

15. Vogel, E.; Hogrefe, F. Angew Chem Int Ed Engl 1974, 13, 735.

16. Hafner, K.; Diehl, H.; Süss, H. U. Angew Chem Int Ed Engl 1976, 15, 104.

17. Hafner, K.; Knaup, G. L. Tetrahedron Lett 1986, 1665.

18. Böttcher, A.; Raabe, G.; Michl, J. J Org Chem 1985, 50, 5050.

19. Gaussian 03, Frisch, M. J.; Trucks, G. W.; Schlegel, H. B.; Scuseria, G. E.; Robb, M. A.; Cheeseman, J. R.; Montgomery, Jr., J. A.; Vreven, T.; Kudin, K. N.; Burant, J. C.; Millam, J. M.; Iyengar, S. S.; Tomasi, J.; Barone, V.; Mennucci, B.; Cossi, M.; Scalmani, G.; Rega, N.; Petersson, G. A.; Nakatsuji, H.; Hada, M.; Ehara, M.; Toyota, K.; Fukuda, R.; Hasegawa, J.; Ishida, M.; Nakajima, T.; Honda, Y.; Kitao, O.; Nakai, H.; Klene, M.; Li, X.; Knox, J. E.; Hratchian, H. P.; Cross, J. B.; Adamo, C.; Jaramillo, J.; Gomperts, R.; Stratmann, R. E.; Yazyev, O.; Austin, A. J.; Cammi, R.; Pomelli, C.; Ochterski, J. W.; Ayala, P. Y.; Morokuma, K.; Voth, G. A.; Salvador, P.; Dannenberg, J. J.; Zakrzewski, V. G.; Dapprich, S.; Daniels, A. D.; Strain, M. C.; Farkas, O.; Malick, D. K.; Rabuck, A. D.; Raghavachari, K.; Foresman, J. B.; Ortiz, J. V.; Cui, Q.; Baboul, A. G.; Clifford, S.; Cioslowski, J.; Stefanov, B. B.; Liu, G.; Liashenko, A.; Piskorz, P.; Komaromi, I.; Martin, R. L.; Fox, D. J.; Keith, T.; Al-Laham, M. A.; Peng, C. Y.; Nanayakkara, A.; Challacombe, M.; Gill, P. M. W.; Johnson, B.; Chen, W.; Wong, M. W.; Gonzalez, C.; Pople, J. A. Gaussian 03, Gaussian: Pittsburgh, 2003.

20. Schäfer, A.; Huber, C.; Ahlrichs, R. J Chem Phys 1994, 100, 5829.

21. Becke, A. D. J Chem Phys 1988, 88, 2547. Becke, A. D. Phys Rev 1988, A38, 3098. Perdew, J. P. Phys Rev 1986, B33, 8822. Perdew, J. P. Phys Rev 1986, B38, 7406.

22. Ahlrichs, R., et al. Turbomole, Version 5; Quantum Chemistry Group, University of Karlsruhe; Karlsruhe, Germany, 1998.

23. Nakatsuji, H. In Computational Chemistry—Reviews of Current Trends, Vol. 2; Lesczynski, J., Ed.; World Scientific: Singapore, 1997; p 62.

24. Dunning, T. H., Jr. J Chem Phys 1970, 53, 2823; Dunning, T. H., Jr.; Hay, P. J. In Methods of Electronic Structure Theory; Schaefer, H. F., III, Ed.; Plenum Press: New York, 1977; p 1; Magnusson, E.; Schaefer, H. F., III, J Chem Phys 1985, 83, 5721.

25. Downing, J.; Ehara, M.; Nakatsuji, H.; Michl, J. (to appear).

26. Warnick, S. M.; Michl, J. J Am Chem Soc 1974, 96, 6280.

27. Kataoka, M.; Koseki, S.; Nakajima, T.; Iida, K. Nouv J Chim 1985, 9, 135.

28. Kitschke, B.; Lindner, H. J. Tetrahedron Lett 1977, 2511.

29. Lindner, H. J.; Kitschke, B. Angew Chem, Int Ed Engl 1976, 15, 106.

30. Stegemann, J.; Lindner, H. J. Tetrahedron Lett 1977, 2515.

31. Vogel, E.; Konigshofen, H.; Wassen, J.; Müllen, K.; Oth, J. F. M. Angew Chem Int Ed Engl 1974, 13, 732.

32. For leading references see Maier, G. Angew Chem, Int Ed Engl 1988, 27, 309. Arnold, B. R.; Michl, J. In Kinetics and Spectroscopy of Carbenes and Biradicals; Platz, M. S., Ed.; Plenum: New York, NY, 1990; Arnold, B. R.; Radziszewski, J. G.; Campion, A.; Perry, S. S.; Michl, J. J Am Chem Soc 1991, 113, 692.

33. Dewar, M. J. S.; Dougherty, R. C. The PMO Theory of Organic Chemistry; Plenum: New York, 1975.

34. Moffitt, W. J Chem Phys 1954, 22, 320, 1820.

35. Except that according to the DFT result, ΣHL is slightly bigger than $|\Delta HSL|$ in **2**.

36. Bonacic-Koutecký, V.; Koutecký, J.; Michl, J. Angew Chem 1987, 99, 216.

37. Döhnert, D.; Koutecký, J. J Am Chem Soc 1980, 102, 1789.